Numerical simulation of a DFB-fiber laser sensor (I)

I. LANCRANJAN[*], S. MICLOS[a], D. SAVASTRU[a]

Advanced Study Center–National Institute of Aerospace Research "Elie Carafoli",
220 Iuliu Maniu Boulevard, Bucharest, Romania
[a] National Institute R&D of Optoelectronics, INOE 2000, 409 Atomistilor str.,
P. O. Box MG. 5, Magurele-Ilfov, Romania

This paper is the first part of a series pointing to numerical simulation of various aspects of distributed feedback fiber laser sensors and their applications. The developed numerical analysis has the scope of a better understanding of DFB-FL itself and of its interaction with environment in order to be operated as a sensor. The aeronautical applications of DFL-FL sensors constitute the main field of numerical simulations and analysis field.

1. Introduction

This paper is the first one of a series pointing to reach an improved design of fiber optic sensors used for various applications, mainly aeronautical. Distributed feedback fiber lasers (DFB-FL) and distributed Bragg reflector fiber lasers (DBR-FL) are the main investigated sensor devices. Distributed feedback fiber lasers (DFB-FL) and distributed Bragg reflector fiber lasers (DBR-FL) possess certain unique properties that make them quite attractive for a number of different applications. They are inherently fiber compatible, and very simple passive thermal stabilization is sufficient to ensure the stability of the laser.

A number of different active dopants, such as erbium, ytterbium, neodymium, and thulium, can be used in order to cover different windows of the optical spectrum. These features, combined with the ability to define the emitted wavelength precisely through the grating structure along with the narrow linewidth and low relative intensity noise (RIN), make DFB-FL and DBR-FL very advantageous for telecommunication applications [1]–[3]. In addition, a number of DFB fiber lasers can be configured in a parallel array to provide flexibility in pumping conditions and provide pump redundancy [2], [4].

Robust single polarization and narrow linewidth of DFB lasers are very desirable for sensor systems [5]–[7]. Alternatively, DFB lasers can be made to operate in stable dual polarization so that simultaneous measurements can be carried out [8]–[10]. In addition to the sensing and telecom applications, DFB fiber lasers suitable for high-power applications have been demonstrated [11].

2. Specification of DFB-FL and DBR-FL sensor application

An important aeronautical application of fiber optic sensors consists in determination of **transition zone** between **laminar** and **turbulent flow** of air along the wing surface. Intermittent regime occurring in-between these two regions (transition) is characterized by turbulent bursts in laminar flow.

The basic idea of this type of measurement is to evaluate the pressure variation in the two zones:

1. Laminar flow - relative constant value of air static pressure, low frequency (~ 100 Hz) and small amplitude ($\Delta P \sim 1$ Pa) pressure variations.

2. Turbulent flow - larger and nonstationary value of air static pressure, higher frequency (~ 10 kHz) and higher amplitude ($\Delta P \sim 10$ Pa) pressure variations.
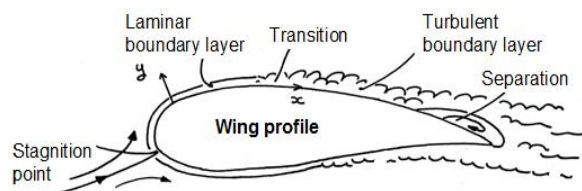

Fig. 1. Schematic representation of the main investigated aeronautical application of DFB-FL and DBR-FL.

The main investigated aeronautical DFB-FL and DBR-FL sensors application consists in determination of the transition zone (line) between laminar and turbulent air flow along the aircraft wing surface. The laminar and turbulent boundary layers can be observed in Fig. 1.

Possible fiber optic "reaction": linear glass strain deformation (glass Young's modulus of elasticity is $E = 50 \div 90 \cdot 10^9$ N/m^2) under air turbulent pressure bursts (deformations of $10^{-9} \div 10^{-8}$ m) is extremely difficult to measure even by optical interferometer methods. In this situation micro-bending of fiber optic appears to be more feasible

deformation as an effect of turbulent air flow pressure bumps.

Schematic representation of the main investigated aeronautical application of DFB-FL and DBR-FL is presented in Fig. 2. The laminar and turbulent air flow zones along the aircraft wing surface are indicated. One possible position of the fiber optic sensor can be observed.
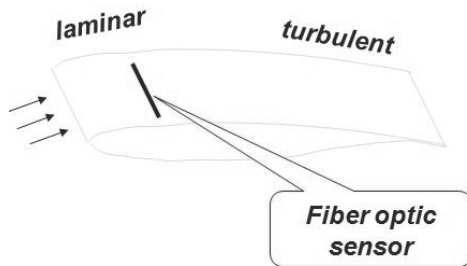

Fig. 2. Schematic representation with few relevant insights of the main investigated aeronautical application of DFB-FL and DBR-FL.

In Fig. 3 it can be observed that the fiber optic sensor is embedded close (0.2 mm depth) to the wing surface. The fiber optic sensor is placed into a soft material, like paraffin, under an 0.2 mm thick aluminum foil.
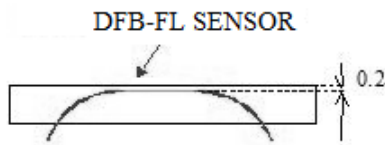

Fig. 3. Insights of one possible way of mounting the DFB-FL and/or DBR-FL in the wing for determination of transition zone between laminar and turbulent air flow along the aircraft wing surface.

One possible procedure for reading the fiber optic sensor is presented schematically in Fig. 4. This possible procedure is based on precise evaluation of lasing wavelength, lasing, which depends on the laser resonant cavity length.
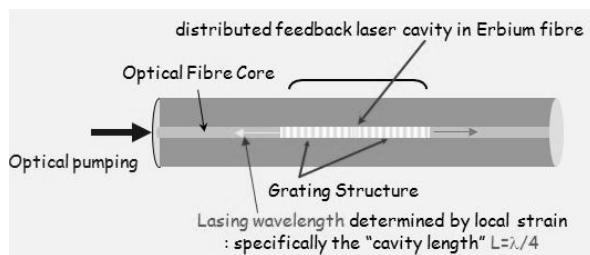

Fig. 4. Some insights about the structure of the DFB-FL and/or DBR-FL proposed to be used for the determination of the transition zone between laminar and turbulent air flow along the wing surface.

Some additional insights about the structure of the DFB-FL and/or DBR-FL proposed to be used for the determination of the transition zone between laminar and turbulent air flow along the wing surface are displayed in Fig. 5. The possible fiber optic sensor output reading by measuring the lasing wavelength shift ($\Delta\lambda$) is indicated.

It is to be noted the role of pumping wavelength used for DFB-FL or DBR-FL. This output reading is applicable for both diode pumping wavelengths, namely 980 nm or 1480 nm. The first one, 980 nm wavelength, is more efficient than the second but has lower saturation intensity. The second one, 1480 nm wavelength, seams to be more interesting for sensor application because its more extended linearity response domain.

An important observation is that the pressure bumps of the turbulent air flow can be recorded by DFB-FL or DBR-FL in two possible ways:
- in the Bragg grating zone;
- in the zone between two successive such Bragg gratings.

3. DFB-FL and DBR-FL sensor architecture.

Regarding the Distributed Feedback Fiber Laser (DFB-FL) and Distributed Bragg Reflector Fiber Laser (DBR-FL) sensors architecture the following are to be observed:

- Both are built using single-mode optical fiber (core of 5 - 10 μm diameter and clad of 80 - 100 μm overall diameter)
- Both are built using single-mode optical fiber as active medium. The active medium is formed by doping the core of the optical fiber with erbium ions (Er^{3+})

The important feature consists in the Bragg grating – spatial sinusoidal refractive index variation in and along the core of the optical fiber. Bragg grating characteristic parameters are: Λ - the wavelength of spatial modulation of the refractive index, λ_B – the Bragg wavelength (defined as $2 \cdot n_{eff} \cdot \Lambda$, the wavelength of maximum reflection coefficient), n_{eff} – the effective value of the refractive index, corresponding to the fundamental mode of electromagnetic field propagation into the optical fiber, being imposed by the geometric characteristics of the optic fiber)
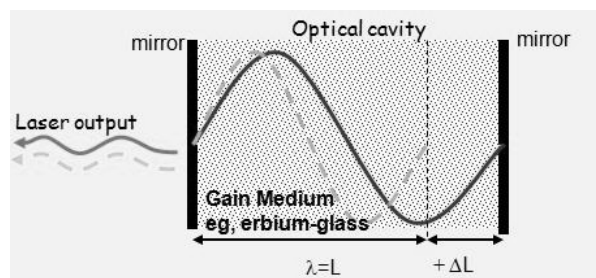

Fig. 5. The possible fiber optic sensor output reading by measuring the lasing wavelength shift ($\Delta\lambda$).

DBR-FL means a laser oscillator formed by the optical fiber active medium placed between two mirrors Bragg gratings (distributed reflector);

DFB-FL means a laser oscillator formed by the optical fiber active medium support of the Bragg grating.

In addition to the structure presented in Fig. 4, some additional insights about the structure of the DFB-FL and/or DBR-FL proposed to be used for the determination of the transition zone between laminar and turbulent air flow along the wing surface are displayed in Figs. 6 and 7.
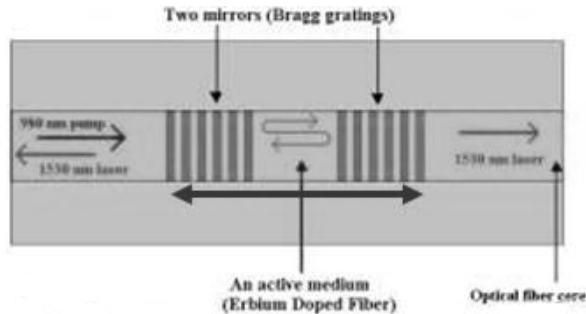

Fig. 7. The possible fiber optic sensor output reading by measuring the lasing wavelength shift (Δλ).

4. DFB-FL theory

Traditionally, there have been three main DFB laser cavity designs that offer different performance and distinctive operational characteristics, presented in the followings.

It was recently shown that the classic parametric optimization approach for a DFB laser, i.e., the definition of the optimum resonator geometry and dimensional values, is analogous to Rigrod optimization [18] of reflectivities in Fabry–Pérot laser cavities of fixed length. It can also be shown that it is possible to further improve the DFB laser efficiency by increasing the effective cavity length without changing the total device length and optimum reflectivities, using a step-apodized profile.

Both optimization approaches are parametric in nature. The main cavity features are defined a priori, and their parameters are continuously varied until a maximum efficiency is reached. However, neither approach guarantees that the ultimate, i.e., maximum possible, efficiency for the given medium has been achieved. In this paper, a drastically different approach is followed.

New method follows an "inverse scattering" philosophy in that, for a given medium and pumping arrangement, it first derives the maximum possible efficiency and the use of the developed algorithm defines the required generalized DFB cavity. This is achieved without any significant a priori assumptions about the grating characteristics. Taking into account the local pump power, the method relies on the calculation of the optimum intracavity signal distribution that results at maximum pump-to-signal conversion at every point along the cavity.

Using this information, the developed algorithm calculates the required grating strength distribution that re-

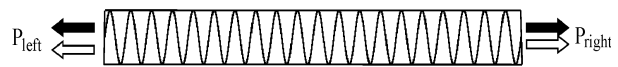sults in the desired optimum signal, pump, and gain distribution.

Fig. 8. Refractive index profile for conventional DFB laser designs. The classic design and two-wavelength bidirectional operation.

The classic design and two-wavelength bidirectional operation is displayed in Fig. 8. It consists of a uniform refractive index grating, with constant amplitude and constant period, incorporated in an active medium. This type of DFB laser operates at two fundamental longitudinal modes at different wavelengths, corresponding to the edges of the grating bandgap, and gives symmetric output powers from both ends, which are equally divided between these two modes [12]. Such a cavity provides dual-wavelength bidirectional operation.
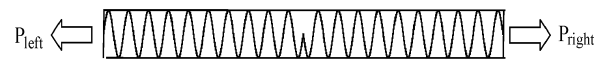

Fig. 9. Refractive index profile for conventional DFB laser designs. Symmetric -phase shifted design and single-wavelength bidirectional operation

Fig. 9 shows the symmetric-phase shifted design and single-wavelength bidirectional operation. In practice however, single-wavelength operation is desirable. This is achieved by introducing a π–shift in the spatial phase of the grating [13]–[15]. If the phase shift is located in the middle of the grating due to the symmetry of the cavity, the output powers at both ends are equal. Such a cavity provides single-wavelength operation, coinciding with the grating Bragg wavelength, and bidirectional operation.
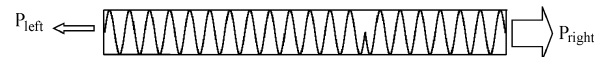

Fig. 10. Refractive index profile for conventional DFB laser designs. Asymmetric π-phase-shifted design and single-wavelength unidirectional operation.

Asymmetric π-phase-shifted design and single-wavelength unidirectional operation is shown in Fig. 10. In addition to single-wavelength emission, unidirectionality is a very desirable feature of high-performance lasers. By placing the phase shift asymmetrically with respect to the grating center, as shown in Fig. 1(c), larger output power is obtained from the shorter end [10], [16]. In this asymmetric design, the maximum output power from the desired end is obtained for a particular phase-shift position and coupling coefficient value. Optimum values of pa-

rameters and are found by varying them over a defined range, either by simulation or by experiment.
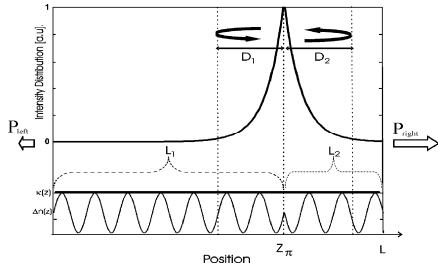

Fig. 11. Standard asymmetric DFB-FL structure.

Standard asymmetric DFB-FL structure is illustrated in Fig. 11 and 12. The optimum position of the π-phase shift position (z_p) can be observed. D_1 and D_2 represent the "penetration" depth of electromagnetic field into the Bragg grating zones.

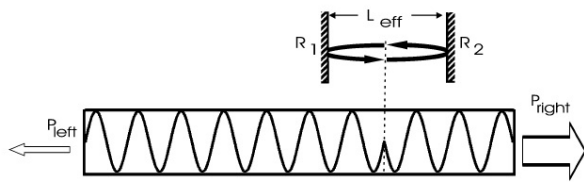*Fig. 12. Standard asymmetric DFB-FL structure. Leff represents the sum of the electromagnetic field penetration depth into Bragg gratings.*

In Fig. 13 is presented Apodized standard asymmetric DFB-FL structure. L_{eff} represents the sum of the electromagnetic field penetration depth into Bragg gratings. Apodization consists in modification of refractive index spatial modulation depth (amplitude).
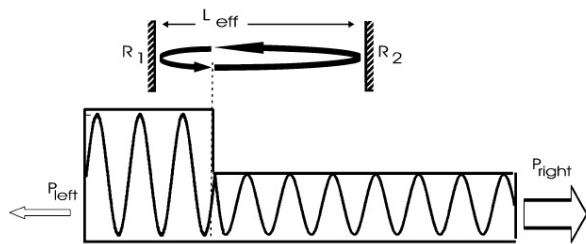

Fig. 13. Apodized standard asymmetric DFB-FL structure.

The standard coupled-mode equations for counterpropagating fields are used (see, e.g., [20]). The electric field (E) is the sum of two counterpropagating fields (A and B).

The forward-propagating field amplitude equation of propagation is given by equation:

$$\frac{dA(z)}{dz} = \alpha(z)A(z) + \kappa(z)B(z)e^{i\Gamma(z)} \qquad (1)$$

The backward-propagating field amplitude equation of propagation is:

$$\frac{dB(z)}{dz} = -\alpha(z)B(z) + \kappa(z)A(z)e^{-i\Gamma(z)} \qquad (2)$$

where $A(z)$ is the amplitude of the forward-propagating field, $B(z)$ is the amplitude of the backward-propagating field, $A(z)e^{-i\beta z}$ represents the envelope of the forward-propagating field, $B(z)e^{i\beta z}$ represents the envelope of the backward-propagating field while β is the unperturbed waveguide mode.

A schematic representation of coupled-mode procedure/method, used for numerical evaluation of DFB-FL structure is presented in Fig. 14.
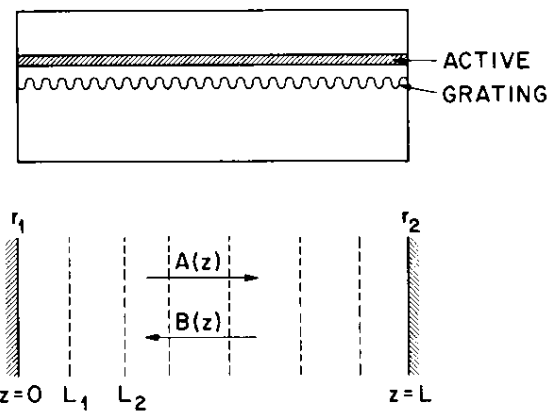

Fig. 14. Schematic representation of coupled-mode procedure/method

Designating by α (z) the net field gain including the background loss and ϕ (z) the Bragg grating phase, the spatial phase factor/coefficient Γ (z) will be given by this equation:

$$\Gamma(z) = 2\beta(z) - \phi(z) \qquad (3)$$

The equation defining the Bragg grating phase ϕ (z) is:

$$\phi(z) = \int_0^z \frac{2\pi}{\Lambda(z^*)} dz^* \qquad (4)$$

where Λ (z) represents the local grating period. The average signal intensity definition is:

$$S(z) = A^2(z) + B^2(z) \qquad (5)$$

while the definition of the intensity difference between the counterpropagating fields is:

$$D(z) = A^2(z) - B^2(z) \qquad (6)$$

The intensity difference $D(z)$ can be expressed as:

$$D(z) = D(0) + 2\int_0^z \alpha(z^*) \cdot S(z^*) dz^* \qquad (7)$$

The standard coupled-mode propagation equations for counterpropagating fields are can be manipulated to provide expressions for $k(z)$, the coupling coefficient of the electromagnetic field:

$$k(z) = \frac{\dfrac{dS(z)}{2z} - D(z)\alpha(z)}{\cos(\Gamma(z))\sqrt{S^2(z) - D^2(z)}} \qquad (8)$$

The usual DFB laser boundary conditions are:

$$A(0) = B(L) = 0 \qquad (9)$$

The new/transformed DFB laser boundary conditions are:

$$D(0) = -B^2(0) = 0$$
$$D(L) = A^2(L) = S(L)$$

These boundary conditions represent the basis of our design method.

Given $S(z)$, $\alpha(z)$ and $\Lambda(z)$, we can use them to find $D(z)$ and then the required coupling coefficient distribution can be calculated.

$$n(z) = n_0 + \Delta n(z) \cdot \cos(\phi(z)) \qquad (10)$$

The coupling coefficient defines the amount of the periodic perturbation required. If this perturbation is sinusoidal the varying refractive-index modulation in the form is defined by the above equation. n_0 is the effective refractive index and Δn is the modulation amplitude.

The reflection coefficient of a grating with constant gain at the Bragg wavelength is:

$$r = \frac{-k \cdot \sinh(\gamma L)}{\gamma \cdot \cosh(\gamma L) - \alpha \cdot \sinh(\gamma L)} \qquad (11)$$

Here γ coefficient is $\gamma = \sqrt{k^2 + \alpha^2}$.

The approximation of reflection coefficient of a grating with constant gain at the Bragg wavelength is given by $r \approx -\tanh(kL)$.

The necessary condition for the validation of the above equation is $\alpha \ll k$.

The reflectivity of the Bragg grating is equal to the reflectivity of a passive grating with no gain:

$$R = r^2 \approx \tanh^2(kL) \qquad (12)$$

Due to the distributed nature of the reflection process in gratings, the incident wave penetrates into the grating before reemerging at the front end. It refers to the case of the case of constant gain and at the Bragg wavelength:

$$D = \frac{1}{2} \cdot \frac{\alpha L\left(\dfrac{\tanh(\gamma L)}{\gamma L} - \dfrac{1}{\cosh^2(\gamma L)}\right) + \tanh^2(\gamma L)}{\alpha \cdot \tanh^2(\gamma L) + \gamma \cdot \tanh(\gamma L)}$$

$$D \approx \frac{\tanh(kL)}{2k} = \frac{r}{2k}$$

In the case of a phase-shifted DFB laser, the total length of effective cavity in which the fields are circulating is

$$L_{eff} = D_1 + D_2 \approx \left(\frac{|r_1|}{2k_1} + \frac{r_2}{2k_2}\right) \qquad (13)$$

D_1 and D_2 are the penetration depths into the Bragg grating segments on the left-hand side and on the right-hand side of the phase shift, respectively.

In the case of a uniform refractive index profile, the coupling coefficient is constant.

5. DBR-FL reflector theory.

A mode propagating on a straight fiber or waveguide fabricated from non-absorbing, non-scattering materials will in principle propagate indefinitely without any loss of power. However, if a bend is introduced, the translational invariance is broken and power is lost from the mode as it propagates into, along and out of the bend. This applies to the fundamental mode in the case of single-mode fibers and waveguides and to all bound modes in the case of bent multimode fibers or waveguides.

Two types of optic fiber bend losses can be considered [20 - 22]:

- Transition loss is associated with the abrupt or rapid change in curvature at the beginning and the end of a bend;

- Pure bend loss is associated with the loss from the bend of constant curvature in between the optic fiber.

The transition loss can be described by an abrupt change in the curvature k from the straight waveguide ($k \sim 0$) to that of the bent waveguide of constant radius R_b ($k = 1/R_b$). The fundamental-mode field is shifted slightly outwards in the plane of the bend, thereby causing a miss-match with the field of the straight waveguide, as presented in Fig. 15.

The fractional loss in fundamental-mode power, $\delta P/P$, can be calculated from the overlap integral between the fields. Within the Gaussian approximation to the fundamental mode field and assuming that the spot size s and core radius or half-width ρ are approximately equal, where V is the fiber or waveguide parameter and D is the relative index difference this gives:

$$\frac{\delta P}{P} \approx \frac{1}{16} \cdot \frac{V^4}{\Delta^2} \cdot \frac{\rho^2}{R_b^2} \qquad (14)$$

Minimizing transition loss can be achieved by considering a number of techniques for significantly reducing transition loss. In the case of planar waveguides it is often possible to fabricate the bend so that there is an abrupt offset between the cores of the straight and bent waveguides in the plane of the bend. In Fig. 15 this can be seen as being equivalent to displacing the bent core downwards so that the two fundamental-mode fields overlap. Alternatively, if a gradual increase in curvature is introduced between the straight and uniformly bent sections, the fundamental field of the straight waveguide will evolve approximately adiabatically into the offset field of the uniformly bent section.
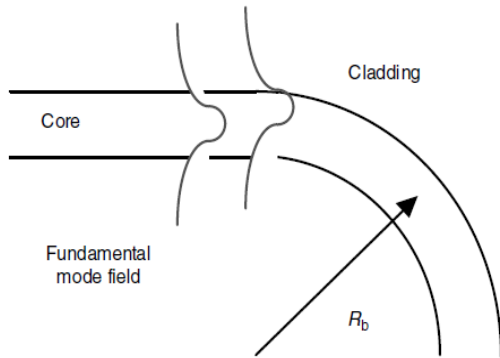

Fig. 15. Outward shift in the fundamental-mode electric field on entering a bend.
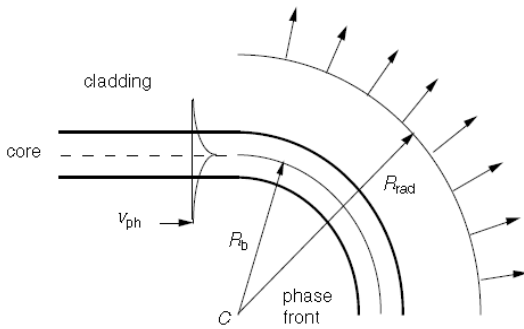

Fig. 16. Schematic of the bending effect of a fiber laser.

The pure bent loss is defined by the fundamental mode continuously optical power loses when propagating along the curved path of the core of constant radius R_b. It is assumed that the cladding is essentially unbounded and not affected by the fiber optic bent, keeping a constant cladding refractive index value, n_{cl}. The radiation loss increases rapidly with decreasing bend radius and occurs predominantly in the plane of the bend; in any other plane the effective bend radius is larger and hence the loss is

very much reduced, as presented in Fig. 16. It has to be observed that the phase velocity anywhere on the modal phase front rotating around the bend cannot exceed the speed of light in the cladding. Hence, beyond radius R_{rad} the modal field must necessarily radiate into the cladding, the radiation being emitted tangentially. The interface between the guided portion of the modal field around the bend and the radiated portion at R_{rad} is known as the radiation caustic, and is the apparent origin of radiation. Between the core and the radiation caustic, the modal field is evanescent and decreases approximately exponentially with increasing radial distance from C. As the bend radius increases, the radiation caustic moves farther into the cladding, and the level of radiated power decreases. R_{rad} can be defined by the equation:

$$R_{rad} = \frac{C}{\Omega \cdot n_{cl}} \qquad (15)$$

The present theoretical analysis is developed by considering step-index optical fibers (with a step profile of the refractive index). In terms of the core and cladding modal parameters U and W, respectively, relative index difference Δ, core radius ρ, fiber parameter V and the bending radius R_b, an approximate expression for γ for the fundamental mode of a step-index fiber has the form [20 - 22]:

$$\gamma = \sqrt{\frac{\pi\rho}{R_b}} \frac{V^2 \sqrt{W}}{2\rho U^2} \exp\left(-\frac{4}{3}\Delta\frac{R_b}{\rho}\frac{W^3}{V^2}\right) \qquad (16)$$

where R_b is necessarily large compared to ρ because it is not possible to bend a fiber into a radius much below 10 mm without breakage. The pure bend loss coefficient is most sensitive to the expression inside the exponent because R_b and ρ. Loss decreases very rapidly with increasing values of R_b or Δ or V (since W also increases with V), and becomes arbitrarily small as R_b tends to infinity.

6. Er^{3+} doped fiber amplifier theory

In this section we will develop and review the fundamentals needed to model an important issue of DFB-FL and DBR-FL namely the laser signal gain in erbium-doped fiber amplifiers. We will build on this foundation, to perform gain and noise modeling of the amplifiers. The underpinning of the gain process consists of coupled atomic population and light flux propagation equations. We will treat the three-level system appropriate for erbium-doped fiber amplifiers at 1.5 mm, We will discuss calculations of the gain in both the small signal and saturation regimes to reach an intuitive understanding of the gain process. Then we will show how the three-level system can be reduced, with certain assumptions, to an equivalent two-level system. The importance of the absorption and emission cross sections, and the difference between the two at a given transition wavelength, will be highlighted. We will cover the concept of the overlap parameter, representing the geometric overlap between the transverse erbium ion dis-

tribution and the transverse profile of the light intensity. We will then outline the importance of amplified stimulated emission and the fundamental mechanism by which it is intertwined into all aspects of the amplification process. Finally, we will discuss analytical models of the erbium-doped fiber.

Three-Level Rate Equations

The most simple treatment of the erbium-doped fiber amplifier starts out by considering a pure three-level atomic system. Most of the important characteristics of the amplifier can be obtained from this simple model and its underlying assumptions.

Setting Up the Three-Level Rate Equations System

We consider a three-level system as depicted in Fig. 17, with a ground state denoted by 1, an intermediate state labeled 3 (into which energy is pumped), and state 2. Since state 2 often has a long lifetime in the case of a good amplifier, it is sometimes referred to as the metastable level. State 2 is the upper level of the amplifying transition and state 1 is the lower level. The populations of the levels are labeled N_1, N_2, and N_S. This three-level system is intended to represent that part of the energy level structure of that is relevant to the amplification process. To obtain amplification, we need a Er^{3+} population inversion between states 1 and 2, and since state 1 is also the ground state, at least half of the total population of erbium ions needs to be excited to level 2 to have population inversion. This raises the threshold pump power needed for amplification and is a known drawback of three-level laser and amplifier systems. One can take particular advantage, in the case of the erbium-doped fiber amplifier, of the fact that the light fields are confined in a very small diameter.
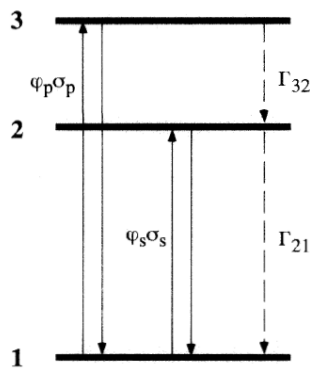

Fig. 17. The Er^{3+} ions characteristic three-level system used for numerical simulation of the amplifier model.

The transition rates between levels 1 and 3 are proportional to the populations in those levels and to the product of pump flux φ_p and pump radiation absorption cross section σ_p. The transition rates between levels 1 and 2 are proportional to the populations in those levels and to the product of signal flux φ_s and signal radiation cross section σ_s. The spontaneous transition rates of the Er^{3+} ions (including radiative and nonradiative contributions) are given by Γ_{32} and Γ_{21}.

In Fig. 18 is presented the energy level structure of Er^{3+} ions. The levels with energy higher than that of $^4I_{13/2}$ level form the pump band. The $^4I_{15/2}$ level forms the ground laser level. The $^4I_{13/2}$ level forms the upper laser level.

The absorption spectrum of the Er^{3+} used as glass doping is shown is Fig. 19. The maximum absorption wavelength of ~980 nm and ~1480 nm can be observed.

The variation of Erbium upper laser level $^4I_{13/2}$ lifetime versus Er^{3+} concentration is presented in Fig. 20. For the optical fiber active media of interest, this lifetime is about ~10 ms.
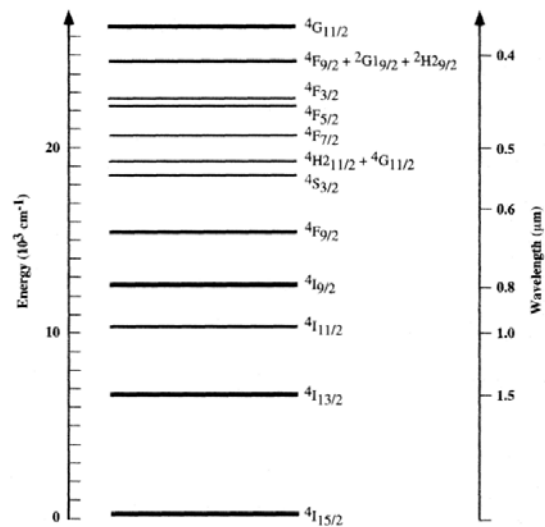

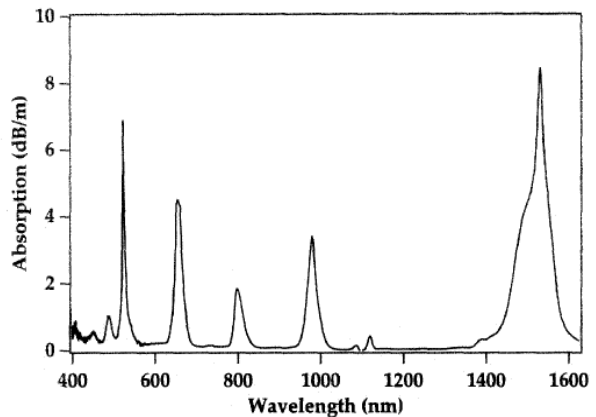*Fig. 18. Energy level structure of Er^{3+} ions.*

Fig. 19. The absorption spectrum of the Er^{3+} used as glass doping.
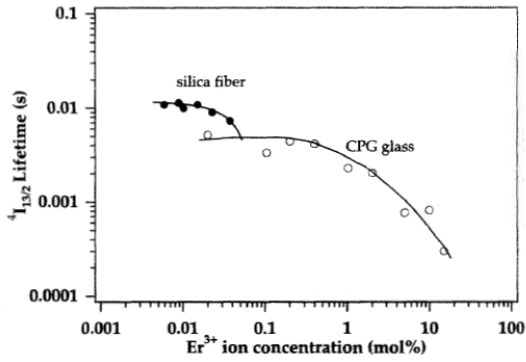
Fig. 20. The variation of Erbium upper laser level $^4I_{13/2}$ lifetime versus Er^{3+} concentration.
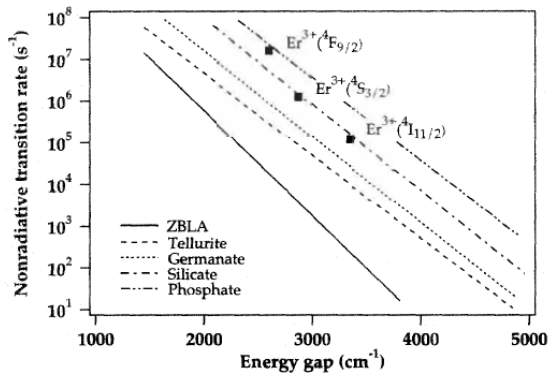

Fig. 21. The nonradiative transition rates of the Er^{3+} ions energy levels of the pump band to the upper laser level.
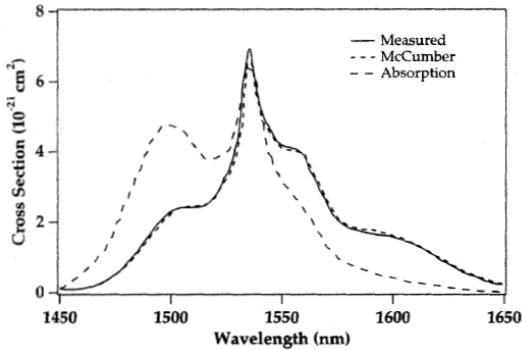

Fig. 22. The spectral distribution of emission cross section of Er^{3+} ions.

7. Numerical simulation results.

Two numerical simulation procedures were used:
- one relaying on MATLAB - MuPAD software package, based on the above mentioned equations;
- the second one relaying on COMSOL software packages.

Numerical simulations were performed for optical fiber with and without doping with erbium ions (Er3+). No significant differences were observed for doped or undoped optical fibers. The numerical simulations were performed using 1.550 µm as the laser wavelength.

In the first stage, transition loss was simulated. Using Eq. (14) relative input power variation was calculated as:

$$P_{rel} = \frac{V^4}{16 \cdot \Delta^2} \cdot \frac{\rho^2}{R_b^2} \qquad (17)$$

where $\rho = 5$ µm is the core radius, $R_b = 5$ mm is the radius of curvature, while Δ – relative index difference and V – modal parameter are calculated as it follows:

$$\Delta = \frac{n_{core}^2 - n_{clad}^2}{n_{core}^2} \qquad (18)$$

$$V = \frac{2\pi \cdot \rho}{\lambda} \sqrt{n_{core}^2 - n_{clad}^2} \qquad (19)$$

$n_{core} = 1.4457$ is the refractive index of the core, with a diameter of 10 µm, $n_{clad} = 1.4378$ is the refractive index of the cladding with an external diameter of 80 µm, while $\lambda = 1.55$ µm denotes the wavelength.

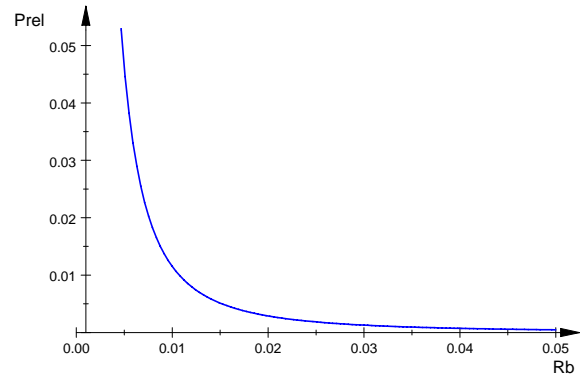Fig. 23 illustrates the variation of P_{rel} vs. R_b.

Fig. 23. The variation of the relative input power against the radius of curvature.

The numerical simulation performed using COMSOL Multiphysics is aiming to obtain an insight on the laser intensity distribution across the transverse section of the optic fiber. The option **2D** was used for the **Space Dimension**. Then the **RF Module** -> **Perpendicular Waves** -> **Hybrid-Mode Waves** -> **Mode analysis** options was used. The geometry of the transverse optical fiber cross section was developed considering realistic parameters. Elliptical deformation of the optical fiber was considered in order to resemble the bend.

Only numerical simulation of single mode optical fiber was considered. The developed geometry of the studied optical fiber was as realistic as possible. Nevertheless only axis symmetric optic fiber was considered. This means that, at this stage of development of DFB-FL and DBR-FL numerical simulation the point-by-point description of transverse fiber optic profile was neglected. In the furure stage of development this more realistic geometry will be considered.
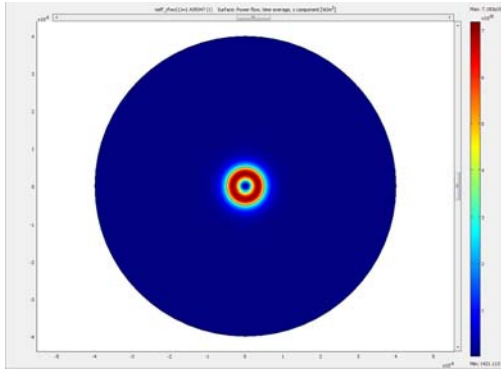
Fig. 24. The numerical simulated time averaged laser power flow across the transverse section of a single mode optical fiber with a core of 10 µm diameter and a cladding of an overall 80 µm diameter.
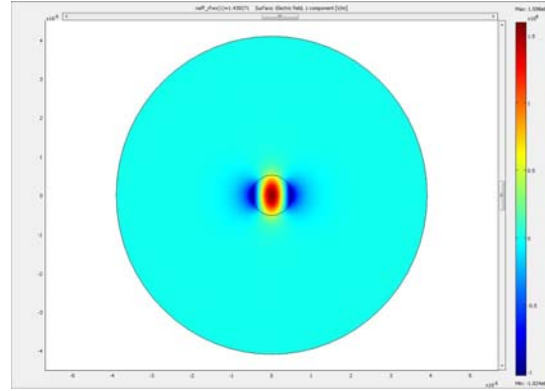

Fig. 25. The numerical simulated time averaged laser electric field distribution into the transverse section of a singlemode optical fiber with a core of 10 µm diameter and a cladding of an overall 80 µm diameter.

Fig. 26. The numerical simulated time averaged laser power flow across the transverse section of a single mode optical fiber with a core of 8.82 µm and 11.33 µm axes and a clad of 70.59 µm and 90.67 µm axes.
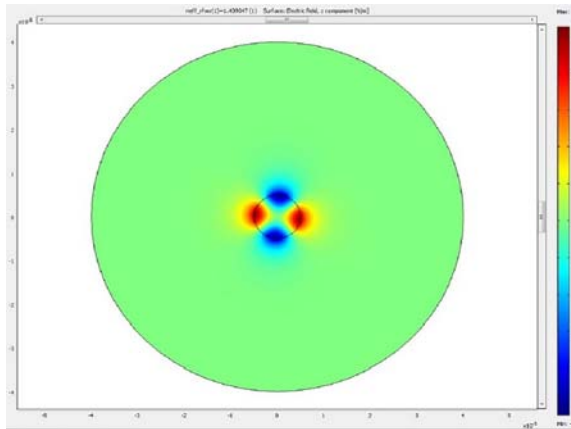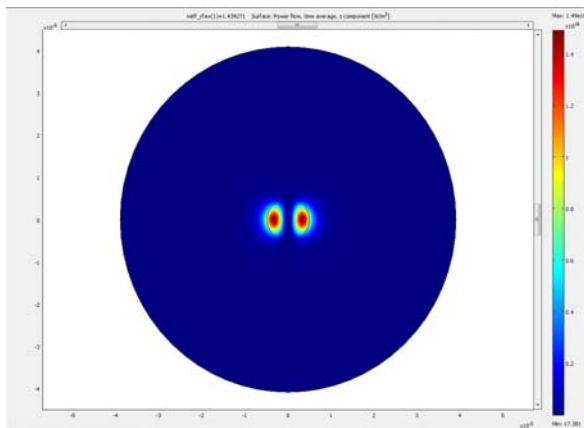

Fig. 27. The numerical simulated time averaged laser electric field distribution into the transverse section of a singlemode optical fiber with a core of 8.82 µm and 11.33 µm axes and a clad of 70.59 µm and 90.67 µm axes.

The procedure tried during numerical simulation consists in considering the laser beam propagation along the bending such as the optical fiber appears as of an elliptical cross section. The deformation was considered by imposing a mechanical stress/pressure on the external surface of the plastic protection layer deposited on the glass cladding. The deformation is expressed in µm. The deformed dimensions of the glass clad and core (the ellipse axes) are calculated as the density is constant. The maximum value of the considered plastic layer deformation (denoted as strain) was of 20 µm.
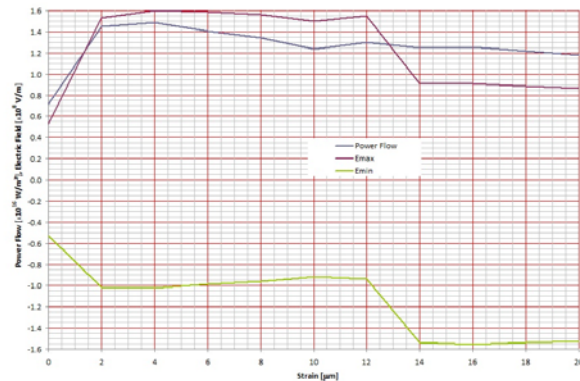

Fig. 28. Variations with strain [mm] of maxim laser field power flow, maximum (E_{max}) and minimum (E_{min}) values of laser electric field.

8. Conclusions

The results of the DFB-FL sensor simulation proves that we obtained a realistic model of the sensor. The effects of the mechanical deformation (bending the optical fiber) were put in evidence. Figures 24-27 reveal that important modifications in laser power flow and electric field distributions appear as effect of microdeformations applied to the studied optical fiber.

The presented results concerning the numerical simulation of DFB-FL and DBR-FL will be further developed.

References

[1] J. Hubner, P. Varming, M. Kristensen, Electron. Lett., **33**(2), 139 (1997).

[2] M. Ibsen, S. U. Alam, M. N. Zervas, A. B. Grudinin, D. N. Payne, IEEE Photon. Technol. Lett. **11**(9), 1114 (1999).

[3] H. N. Poulsen, P. Varming, A. Buxens, A. T. Clausen, P. Munoz, P. Jeppesen, C. V. Poulsen, J. E. Pedersen, L. Eskildsen, "1607 nm DFB fiber laser for optical communcation in the L-band," presented at the Eur. Conf. Optical Communications (ECOC), Nice, France, Sep. 26–30, 1999, Paper MoB2.1.

[4] L. B. Fu, R. Selvas, M. Ibsen, J. K. Sahu, J. N. Jang, S. U. Alam, J. Nilsson, D. J. Richardson, D. N. Payne, C. Codemard, S. Goncharov, I. Zalevsky, A. B. Grudinin, IEEE Photon. Technol. Lett **15**(5), 655 (2003).

[5] Z. E. Haratjunian, W. H. Loh, R. I. Laming, D. N. Payne, Electron. Lett., **32**(4), 346 (1996).

[6] H. Storoy, B. Sahlgren, and R. Stubbe, Electron. Lett. **33**(1), 56 (1997).

[7] J. L. Philipsen, M. O. Berendt, P. Varming, V. C. Lauridsen, J. H. Povlsen, J. Hubner, M. Kristensen, B. Palsdottir, Electron. Lett. **34**(7), 678 (1998).

[8] J. T. Kringlebotn, W. H. Loh, R. I. Laming, Opt. Lett., **21**(22), 1869 (1996).

[9] O. Hadeler, E. Ronnekleiv, M. Ibsen, R. I. Laming, Appl. Opt., **38**(10), 1953 (1999).

[10] O. Hadeler, M. Ibsen, M. N. Zervas, Appl. Opt. **40**(19), 3169 (2001).

[11] C. A. Codemard, L. Hickey, K. Yelen, D. B. S. Soh, R.Wixey,M. Coker, M. N. Zervas, J. Nilsson, "400 mW 1060 nm ytterbium doped fiber DFB laser," presented at the Photonics West LASE, San Jose, CA, Jan.24–29, 2004, Paper 5335-11.

[12] H. Kogelnik, C. V. Shank, J. Appl. Phys. **43**(5), 2327 (1972).

[13] J. T. Kringlebotn, J. L. Archambault, L. Reekie, D. N. Payne, Opt. Lett., **19**(24), 2101 (1994).

[14] V. C. Lauridsen, J. H. Povlsen, P. Varming, Electron. Lett., **34**(21), 2028 (1998).

[15] V. C. Lauridsen, J. H. Povlsen, P. Varming, Electron. Lett., **35**(4), 300 (1999).

[16] M. Ibsen, E. Ronnekleiv, G. J. Cowle, M. O. Berendt, O. Hadeler, M. N. Zervas, R. Laming, "Robust high power (>20 mW) all-fiber DFB lasers with unidirectional and truly single polarization outputs,"presented at the Conf. Lasers and Electro-Optics (CLEO), Baltimore, MD, May 1999, Paper CWE4.

[17] K. Yelen, L. M. B. Hickey, M. N. Zervas, IEEE J. Quantum Electron., **40**(6), 711 (2004).

[18] W. W. Rigrod, J. Appl. Phys., **36**(8), 2487 (1965).

[19] G. Morthier, R. Baets, J. Lightw. Technol, **9**(10), 1305 (1991).

[20] A. W. Snyder, J. D. Love, Optical Waveguide Theory (Dordrecht: Kluwer Academic Publishers); 2000

[21] A. W. Snyder, J. D. Love, IEEE Trans Microwave Theory Tech, **23**, 134 (1975).

[22] J. A. Besley, J. D. Love, Supermode analysis of fibre transmission Proc IEE, 144 411 – 419, 1997

_____
[*]Corresponding author: j_j_f_l@yahoo.com